International Journal of Hydrogen Energy 92 (2024) 1099–1107

Contents lists available at ScienceDirect

International Journal of Hydrogen Energy

journal homepage: www.elsevier.com/locate/he

$CoFe_2O_4$ nanoparticle embedded carbon nanofibers: A promising non-noble metal catalyst for oxygen evolution reaction

T.P. Kamble [a], S.R. Shingte [b], V.D. Chavan [c], Deok-Kee Kim [c], S.H. Mujawar [d], T.D. Dongale [a], P.B. Patil [b,*]

[a] School of Nanoscience and Technology, Shivaji University, Kolhapur, Maharashtra, 416004, India
[b] Department of Physics, The New College, Shivaji University, Kolhapur, Maharashtra, 416012, India
[c] Department of Electrical Engineering and Convergence Engineering for Intelligent Drone, Sejong University, Seoul, South Korea
[d] Department of Physics, Yashawantrao Chavan Institute of Science, Satara, Maharashtra, 415001, India

ARTICLE INFO

Handling Editor: Prof. A.B. Basile

Keywords:
MOF
Nanofibers
Cobalt ferrite
Non noble metal catalyst
Oxygen evolution reaction

ABSTRACT

There is a strong demand for noble metal-free durable catalysts to facilitate the advancement of clean, sustainable energy technologies and to replace energy equipment reliant on fossil fuels. In this study, metal-organic framework (MOF)-derived $CoFe_2O_4$ (CFO) nanoparticle-embedded electrospun carbon nanofibers (CNFs) were synthesized. Nanofibers were calcined at three different temperatures to obtain optimum electrocatalytic performance in oxygen evolution reaction (OER). Nanofibers annealed at 800 °C (CFO@CNFs 800) displayed a reduced overpotential of 300 mV while maintaining a steady current density of 10 mA cm^{-2}. CFO@CNFs 800 demonstrated Tafel slope 42 mV dec^{-1} with excellent long-term stability up to 48 h. The synergistic effect of the redox activity of CFO coupled with the high surface area and conductivity of carbon nanofibers is responsible for enhanced OER performance.

1. Introduction

Sustainable progress of human society encounters challenges of the global energy crisis, environmental pollution, and changes in climate patterns [1,2]. Addressing these issues requires sustainable and efficient energy solutions. Hydrogen, a promising contender for the future of sustainable energy, can be generated through environment-friendly photochemical and electrochemical water electrolysis methods [3]. Electrochemical water splitting is of particular interest since photochemical water electrolysis has low efficiency in converting solar energy to hydrogen [4]. Electrochemical water splitting involves two distinct half-reactions: the oxygen evolution reaction (OER) occurring at the anode and the hydrogen evolution reaction (HER) taking place at the cathode [5]. In the context of electrochemical water splitting, researchers commonly utilize five evaluation parameters. These metrics encompass overpotential, Tafel slope, electrochemical active surface area (ECSA), turnover frequency (TOF), and durability studies [6]. Excellent electrocatalysts show lower overpotential, fast kinetics, negligible charge transfer resistance (R_{ct}), a significant ECSA, and large long-term stability. Although platinum (Pt) has traditionally been considered the most efficient electrocatalyst for the HER, however, its high price hinders its practicality for large-scale applications. Numerous studies have investigated the use of non-noble metals, for instance, nickel (Ni), cobalt (Co), iron (Fe), copper (Cu), molybdenum (Mo), and their oxides as potential alternatives to platinum group metals [7].

Within the extensive range of metal oxides, those based on iron ($M^{II}Fe_2O_4$, where $M^{II} = Fe^{2+}$, Co^{2+}, Ni^{2+}, Mn^{2+}) have great redox activity, in addition to being inexpensive, abundant, and environmentally friendly [8]. Due to its stability in a basic environment with efficient electrochemical activity, $CoFe_2O_4$ is suitable for water splitting, especially for OER. Rana et al. used the nanocubes of $CoFe_2O_4$ which shows an overpotential of 430 mV at a current density of 10 mA cm^{-2}, coupled with a Tafel slope of 44 mV dec^{-1} [9]. Li et al. used $MnFe_2O_4$ which achieved an overpotential of 470 mV at 10 mA/cm^2 current density and 114 mV/dec^{-1} [10]. Metal-organic frameworks (MOFs) are renowned for their extensive surface area and customizable porosity, making them ideal porous electrocatalysts [11,12]. However, MOFs typically have low conductivity, which hinders their effectiveness in electrocatalysts. Through heat treatment, the characteristics of MOF-derived composites, including conductivity, stability, pore size, and catalytic activity can be

* Corresponding author.
E-mail address: prashantphy@gmail.com (P.B. Patil).

https://doi.org/10.1016/j.ijhydene.2024.10.353
Received 6 July 2024; Received in revised form 27 September 2024; Accepted 24 October 2024

tuned [13,14]. To increase the catalytic activity for total water splitting, electrocatalysts must also be structurally and morphologically developed. One-dimensional (1D) nanostructures exhibit significant specific surface areas compared to zero-dimensional (0D) and two-dimensional (2D) nanocatalysts depending upon the specific materials, synthesis method, and their structural configurations. With the development of nanotechnology, significant research has been done on the utilization of 1D nanomaterials as electrocatalysts for energy conversion. By engineering the properties of MOFs and exploiting the adaptability of electrospinning precursors, it is possible to create highly efficient electrocatalysts by growing MOF-derived nanoparticles (NPs) directly onto electrospun nanofibers through a facile method. MOF-derived metal oxides offer a high surface area and tunable porosity. When combined with nanofibers, these composites leverage the excellent conductivity and interconnected network structure of the nanofibers. This synergy results in better mass transport and higher electrocatalytic performance.

In this study, we have developed a fibrous network of carbon nanofibers embedded with $CoFe_2O_4$ (CFO) NPs using a combination of hydrothermal and electrospinning techniques. The hydrothermally synthesized CoFe MOF was successfully incorporated into a polymeric matrix through electrospinning. The produced nanofibers were annealed at 600 °C, 700 °C, and 800 °C and denoted as CFO@CNFs 600, CFO@CNFs 700, and CFO@CNFs 800. These catalysts were evaluated for their electrocatalytic performance in the OER. Notably, CFO@CNFs 800 exhibited a significantly lesser overpotential of 300 mV at a current density of 10 mA cm^{-2}. The resulting charge transfer resistance (R_{ct}) and Tafel slope for CFO@CNFs 800 were measured to be 1.5 Ω/cm^2 and 42 mV dec^{-1}, respectively. Furthermore, CFO@CNFs 800 demonstrated excellent stability over a 48 h testing period.

2. Materials and method

2.1. Chemicals

Cobalt nitrate hexahydrate ($Co(No_3)_2.6H_2O$, SRL Pvt Ltd), iron nitrate nonahydrate ($Fe(NO_3)_2{\cdot}9H_2O$, Sigma Aldrich), terephthalic acid (PTA, Sigma Aldrich), polyacrylonitrile (PAN, Sigma Aldrich Mw – 150 000), N, N-dimethylformamide (DMF), potassium hydroxide (KOH, Loba Chemie Pvt Ltd), and double distilled water (DDW) was used for all solution preparations. For electrode preparation, commercial Ni foam, polyvinylidene fluoride (PVDF), activated carbon, and N-methyl-2-pyrrolidone (NMP) were used.

2.2. Synthesis of the CoFe MOF

CoFe MOF was synthesized using a previously described hydrothermal technique with slight changes [15]. For this, 0.145 g of cobalt nitrate hexahydrate and 0.202 g of ferric nitrate nonahydrate were dissolved in 15 ml of DMF. In another 15 ml of DMF, 0.083 g of terephthalic acid was dissolved. Both solutions were mixed and continuously stirred for 30 min to achieve a uniform solution. Afterward, the mixture was put into a stainless-steel autoclave lined with Teflon, which was then maintained at 150 °C for 8 h. After reaching room temperature, brown-colored CoFe MOF powder was obtained through centrifugation, followed by multiple washes with DMF and DDW.

2.3. Synthesis of the MOF-derived $CoFe_2O_4$ NPs embedded carbon nanofibers (CFO@CNFs)

The MOF-derived $CoFe_2O_4$ NPs embedded carbon nanofibers (CFO@CNFs) were produced using a straightforward electrospinning method and subsequent annealing treatment. At first, PAN polymer (0.5 g) was dissolved in 10 ml of DMF with continuous stirring for 4 h. Simultaneously, 4 ml of DMF was used to dissolve CoFe MOF (0.05 g) with constant stirring for 4 h. After that, both solutions were combined and vigorously stirred for 12 h. The final solution was injected into a 20 ml syringe and electrically spun on aluminium foil. The separation between the needle and a rolling collector was 15 cm, with a voltage of 6.1 kV. The flow rate remained constant at 0.2 ml per h^{-1}. Initially, the obtained CoFe MOF embedded on PAN fibers were calcined in the air for 2 h at 240 °C. Then these fibers were immediately annealed in nitrogen for 2 h at 600 °C, 700 °C, and 800 °C with a heating rate of 3 °C min^{-1} and denoted as CFO@CNFs 600, CFO@CNFs 700, and CFO@CNFs 800 (see Fig. 1).

2.4. Electrode preparation

For electrochemical application, the working electrode was fabricated by mixing CFO@CNFs, PVDF, and activated carbon in the weight ratio of 80:10:10 in NMP solvent. The obtained paste was applied to the well-cleaned nickel foam substrate using the brush coating method. The working electrodes were then dried for 12 h at 50 °C.

2.5. Material characterization

X-ray diffraction was conducted using XRD (AXS D8 Advance) with Copper K alpha radiation (λ = ~1.54 A U.) to know about the crystal structure of the prepared sample. The presence of the functional groups was evaluated by Fourier-transform infrared spectroscopy (FTIR) using a Jasco FTIR Spectrometer 4600, Japan. The field emission scanning electron microscope (FESEM, Hitachi SU 8010) was used to characterize the surface morphology of CFO@CNFs. Microstructural characterization and chemical composition analysis were performed with a high-resolution transmission electron microscope (HRTEM, Hitachi/HF-3300 300 kV) coupled to energy-dispersive X-ray spectroscopy (EDS). Elemental chemical states were characterized by X-ray photoelectron spectroscopy (XPS) analysis with a Thermo Fisher Scientific SIGMA PROBE.

2.6. Electrochemical measurements

Electrochemical Characterizations of CFO@CNFs were examined with a Metrohm Autolab PGSTAT204 workstation (NOVA software). In a three-electrode setup, Ag/AgCl (with a 3 M KCl electrolyte) and Pt wire were the reference and counter electrodes. A CFO@CNFs is employed as a working electrode and 1 M KOH was used as an electrolytic solution. Polarization curves for the catalyst electrodes were obtained with Linear sweep voltammetry (LSV). Cyclic voltammetry (CV) measurements were performed to calculate the double-layer capacitances (C_{dl}). Chronopotentiometry (CP) was used to evaluate the stability of the catalysts. The EIS tests were carried out in the range of 10^5–0.01 Hz using a signal amplitude of 10 mV.

3. Results and discussion

3.1. Characterizations

The XRD patterns of all the samples synthesized at various annealing temperatures viz. CFO@CNFs 600, CFO@CNFs 700, and CFO@CNFs 800) are shown in Fig. 2a. All samples exhibit identifiable peaks at 30.14°, 35.49°, 43.13°, 53.58°, 57.11°, and 62.66° corresponding to (220), (311), (400), (422), (511), and (440) lattice planes of $CoFe_2O_4$ with cubic crystal lattice with space group Fd-3m (JCPDS No. 00-002-1045). Further, a small peak at 44.8°, denoted by an asterisk, is indicative of the presence of cobalt with a cubic crystal structure [16]. The peak detected around 22° in CFO@CNFs 600 is from the PAN polymer [15]. This peak broadened and shifted towards higher degrees in CFO@CNFs 700 and CFO@CNFs 800 as the annealing temperature increased owing to the decomposition of the organic ligand forming carbon in a graphitized form. The loss of organic material and the coalescence of crystalline structures at higher annealing temperature has

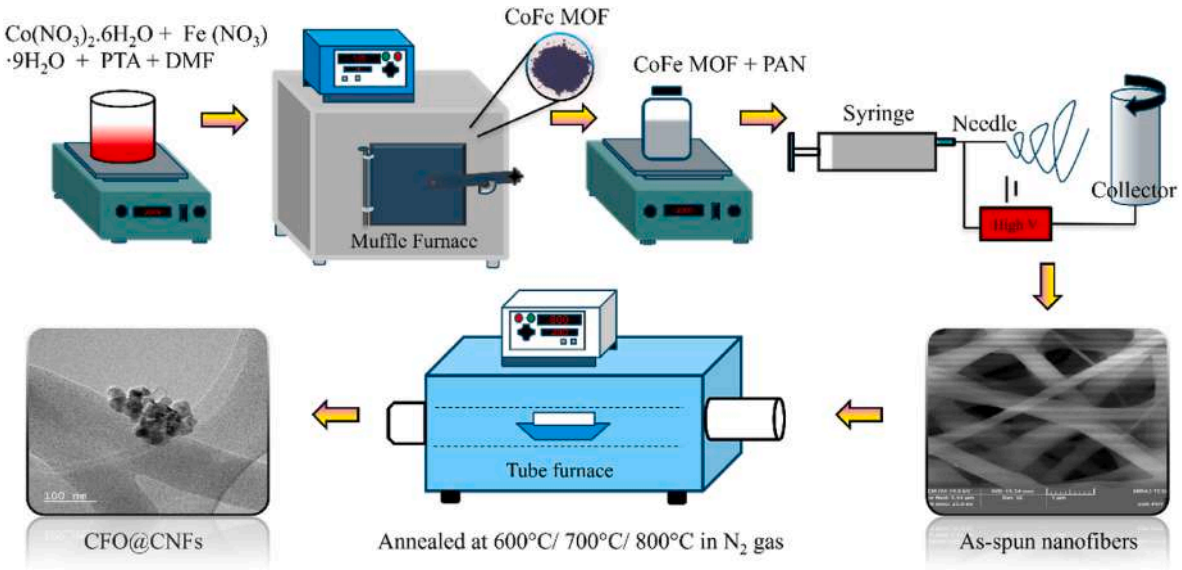

Fig. 1. Schematic of the methodology for the synthesis of CFO@CNFs

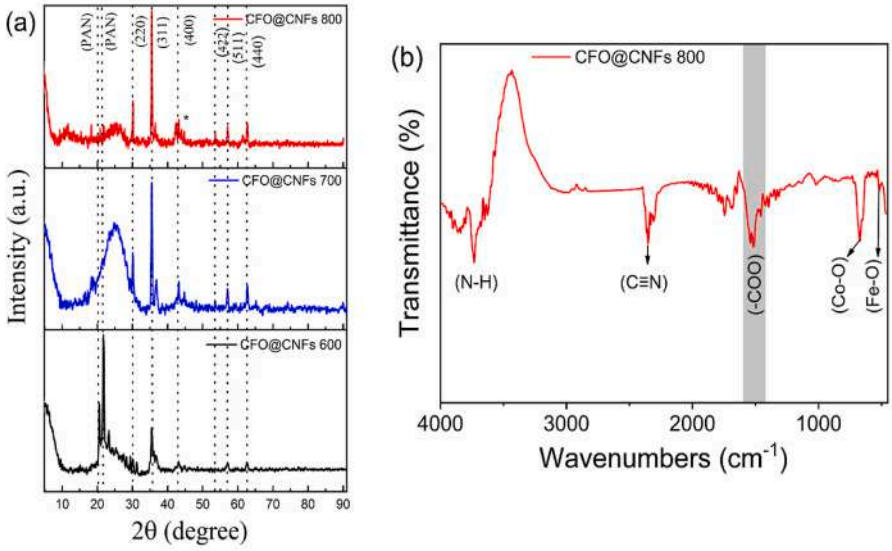

Fig. 2. (a) XRD patterns of CFO@CNFs 600, CFO@CNFs 700, and CFO@CNFs 800. (b) FTIR spectrum of CFO@CNFs 800.

resulted in the reduction of the PAN peak intensity [17]. In comparison to CFO@CNFs 600, the diffraction peaks attributed to CFO become narrower and more intense in CFO@CNFs 700 and CFO@CNFs 800, indicating an improvement in crystallinity as annealing temperature rises. The crystallite size of CFO@CNFs samples was determined by the Scherrer formula using the (311) peak. The crystallite size obtained for CFO@CNFs 600, CFO@CNFs 700, and CFO@CNFs 800 are approximately 25.6 nm, 25.8 nm, and 31.9 nm, respectively. This finding indicates that the $CoFe_2O_4$ grain size increases as the calcination temperature is raised from 600 to 800 °C. The FTIR spectrum of CFO@CNFs 800 (Fig. 2b) illustrates the vibrational frequencies associated with various functional groups. A band at 3725 cm^{-1} corresponding to N–H stretches indicates the presence of hydrophilic functional groups within the carbon network [18]. The absorption peaks at 1537 and 1380 cm^{-1} correspond to the asymmetric and symmetric stretching modes of –COO groups of the H_2BDC ligand. The 677 and 525 cm^{-1} peaks signify Co–O and Fe–O stretching vibrations, respectively [19]. The peak at 2320 cm^{-1} corresponding to the –C ≡ N group appears due to residual PAN [20].

The morphological and microstructural examination of annealed nanofibers was carried out utilizing FESEM and TEM (Fig. 3). The FESEM images (Fig. 3a-c) illustrate the fibrous structure of CNFs on which CFO NPs are dispersed across all annealing temperatures. The low and high-magnification FESEM images of PAN fibers decorated with CoFe MOF before annealing are presented in Fig. S1 of supplementary information (SI). The PAN fibers exhibited an average diameter of ≈900 nm before annealing. Upon annealing, PAN fibers decorated with CoFe MOF were converted into CFO@CNFs of a notably reduced average diameter. The average diameter measured was 152 nm for CFO@CNFs 600, 142 nm for CFO@CNFs 700, and 71 nm for CFO@CNFs 800. The CFO@CNFs 800 experienced a reduction in diameter because of the removal of PAN and the breakdown of the cobalt and ferrite precursors. The TEM images further verify the fibrous structure consisting of CFO NPs (Fig. 3d-f).

The HR-TEM image of CFO@CNFs 800 (Fig. 4a) reveals lattice fringes exhibiting an interplanar spacing of 0.15 nm, corresponding to the (440) planes of $CoFe_2O_4$. Fig. 4b displays a selected area electron diffraction (SAED) pattern indicating the polycrystalline nature of spinel

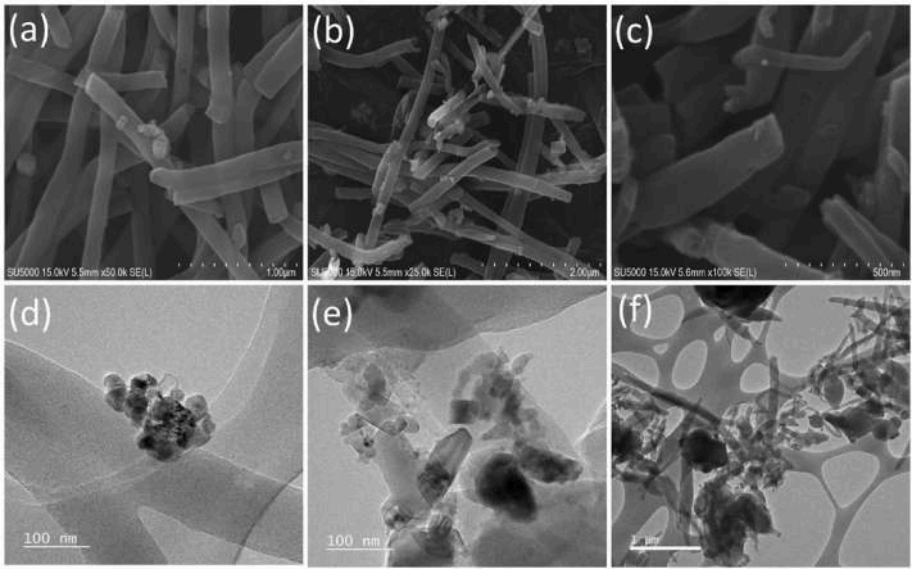

Fig. 3. FESEM (a, b, and c) and TEM (d, e, and f) images of CFO@CNFs 600, CFO@CNFs 700, and CFO@CNFs 800, respectively.

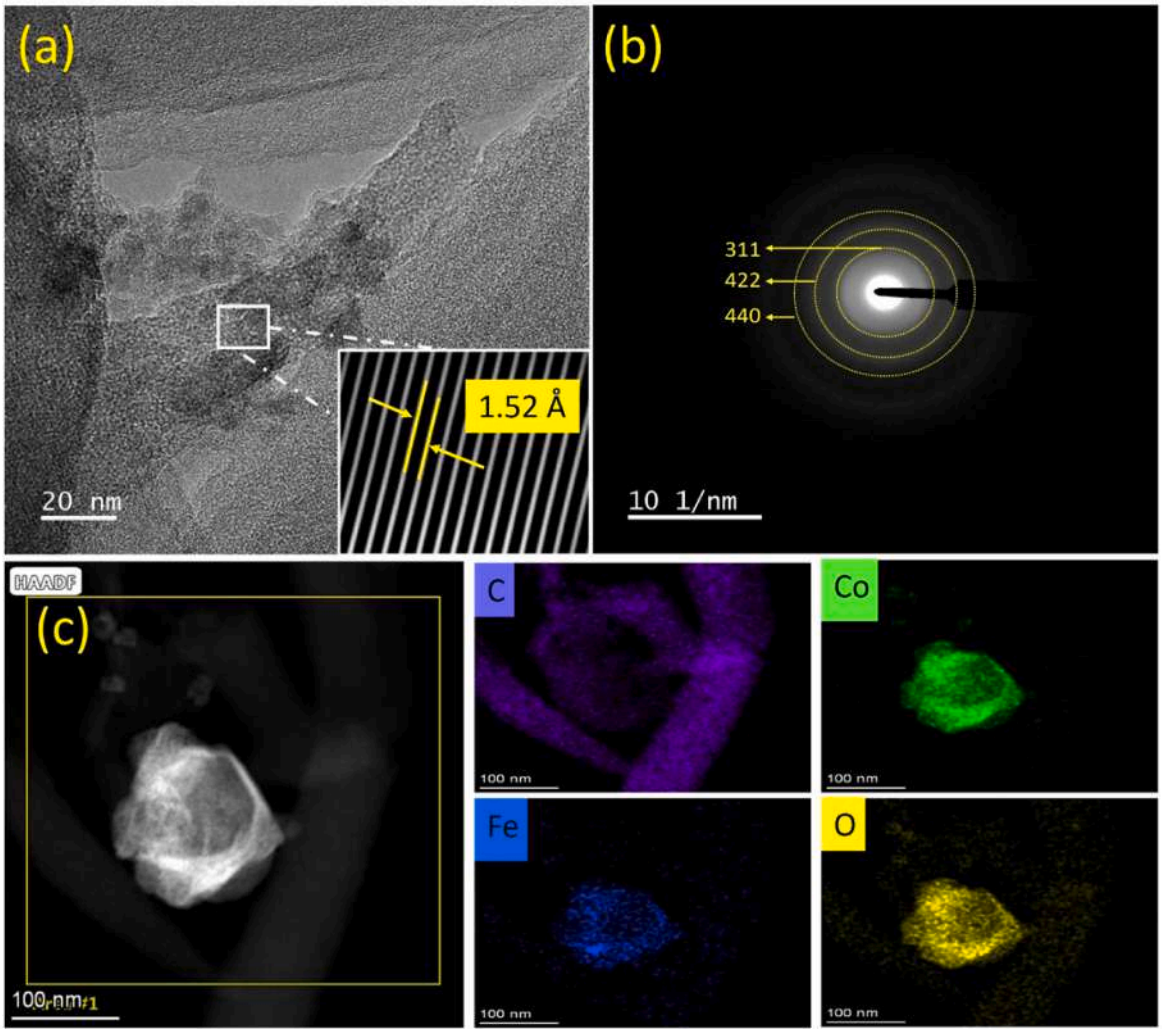

Fig. 4. HR-TEM image (a), SAED pattern (b), and HAADF TEM image and related elemental mapping images (c) of the CFO@CNFs 800.

$CoFe_2O_4$, revealing distinct diffraction rings corresponding to the (311), (422), and (440) planes. In Fig. 4c, the high-angle annular dark field scanning transmission electron microscopic (HAADF STEM) image and EDS elemental mappings of CFO@CNFs 800 are depicted. The elemental mapping confirms the presence of C from CNFs and Co, Fe, and O elements from CFO. Additionally, HR-TEM images, SAED pattern, HAADF STEM images, and related elemental mapping images of the CFO@CNFs 600 and CFO@CNFs 700 are provided in Figs. S2 and S3 of SI.

XPS measurements were performed to examine the valence state and chemical composition of CFO@CNFs 800. The Fe 2p and Co 2p peaks were particularly useful in examining the characteristics of metal ion species within spinel oxide. In the deconvoluted Co 2p spectrum (Fig. 5a) of CFO@CNFs 800, the primary peaks at 780.1 eV (Co $2p_{3/2}$) and 796.1 eV (Co $2p_{1/2}$) were observed for $CoFe_2O_4$ with a spin-orbit separation of 16 eV. Two additional satellite peaks appeared at 802.5 eV and 784.5 eV corresponds to the lower binding energy edge of the Co $2p_{1/2}$ and Co $2p_{3/2}$ peaks, respectively. The presence of shake-up satellite peaks and primary peaks indicates the 2^+ valence state of Co [21, 22]. In the Fe 2p spectrum (Fig. 5b), two obvious peaks at 710.8 eV and 723.6 eV correspond to Fe $2p_{3/2}$ and Fe $2p_{1/2}$, respectively. The peak at 717.2 eV is attributed to a satellite peak. The two principal peaks, featuring a spin-orbit separation of 12.8 eV ascribed to Fe $2p_{3/2}$ and Fe $2p_{1/2}$, reveal that Fe exists in the 3^+ oxidation state [23]. The XPS spectrum of C 1s (Fig. 5c) demonstrates three distinct peaks at 284.4 eV, 285.3 eV, and 288.3 eV corresponding to C–C, C–N, and C–O bonds, respectively. The XPS spectrum of O 1s (Fig. 5d) exhibits two peaks at 531.8 and 533.9 eV indicative of Fe–O/Co–O and C–O, respectively.

3.2. Oxygen evolution reaction of CFO@CNFs catalysts

The electrocatalytic oxygen evolution reaction (OER) activity of CFO@CNFs calcined at various temperatures was investigated in 1 M KOH electrolyte. The OER activity of CFO@CNFs 600, CFO@CNFs 700, and CFO@CNFs 800 samples were assessed through LSV polarization curves in 0–0.8 V voltage regime at 1 mV/s scan rate with iR correction (Fig. 6A). Additionally, LSV polarization curves of all samples without iR correction and corresponding Tafel plots are presented in Fig. S4 of the SI. All measured potentials were converted to potentials relative to the reversible hydrogen electrode (RHE) by employing the Nernst equation [24],

$$E_{RHE} = E_{Ag/AgCl} + 0.059pH + 0.210 \quad [1]$$

where 0.059 is a Faraday constant, and 0.210 is the standard potential of the Ag/AgCl reference electrode. The standard pH value of 1 M KOH solution is 14. The OER onset potentials for the sample CFO@CNFs 600, CFO@CNFs 700, and CFO@CNFs 800 are found to be 1.59 V, 1.57 V, and 1.53 V, respectively. The overpotential required to achieve a current density (j) of 10 mA/cm^2 was determined using equation [25],

$$\eta = V_{RHE} - 1.23\ V \quad [2]$$

here, η represents the overpotential required for electrochemical water-splitting, with 1.23 V being the corresponding voltage value. The overpotential values obtained (with iR correction) for CFO@CNFs 600, CFO@CNFs 700, and CFO@CNFs 800 samples are 350 mV, 340 mV, and 300 mV, respectively. The CFO@CNFs materials exhibit a lower overpotential due to their MOF-derived architecture, which enhances surface area and active sites. Additionally, the one-dimensional fibrous networks contribute to structural uniformity, directional electron flow,

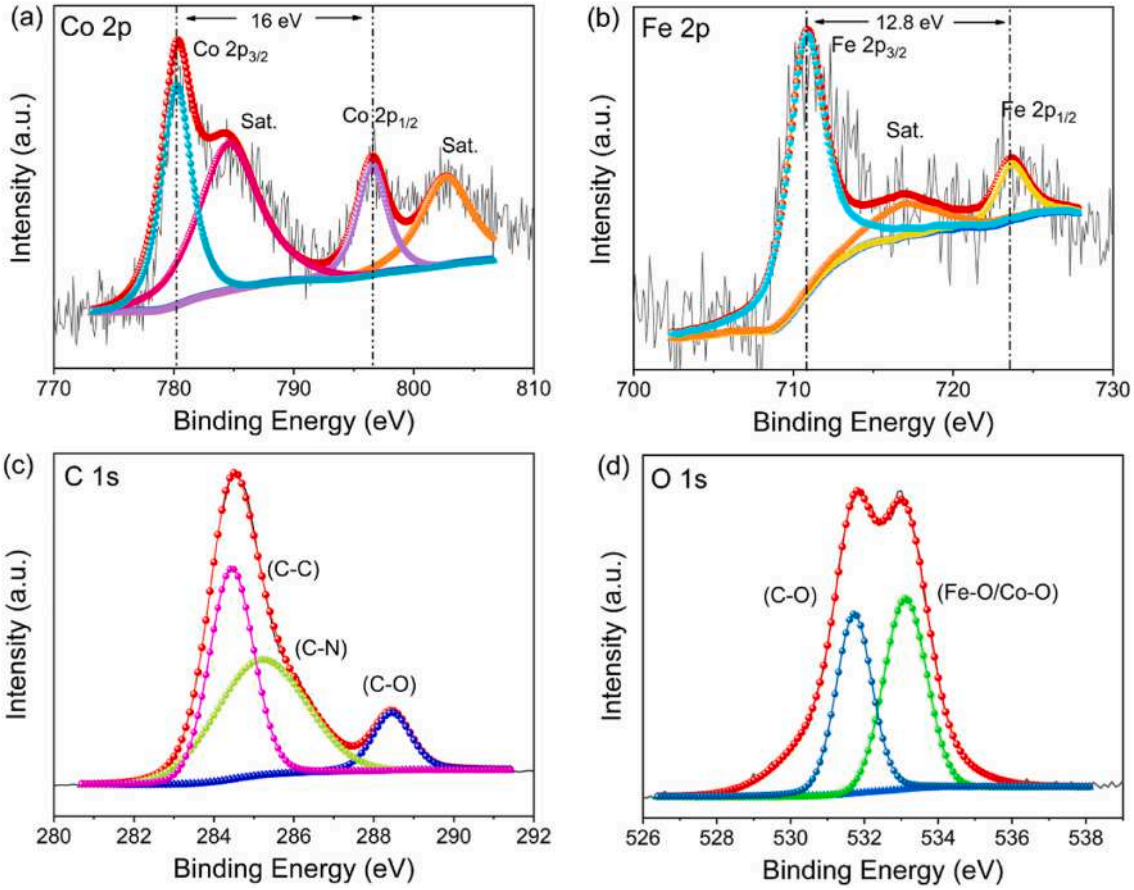

Fig. 5. The deconvoluted XPS spectra for Co 2p (a), Fe 2p (b), C 1s spectra (c), and O 1s (d) of CFO@CNFs 800.

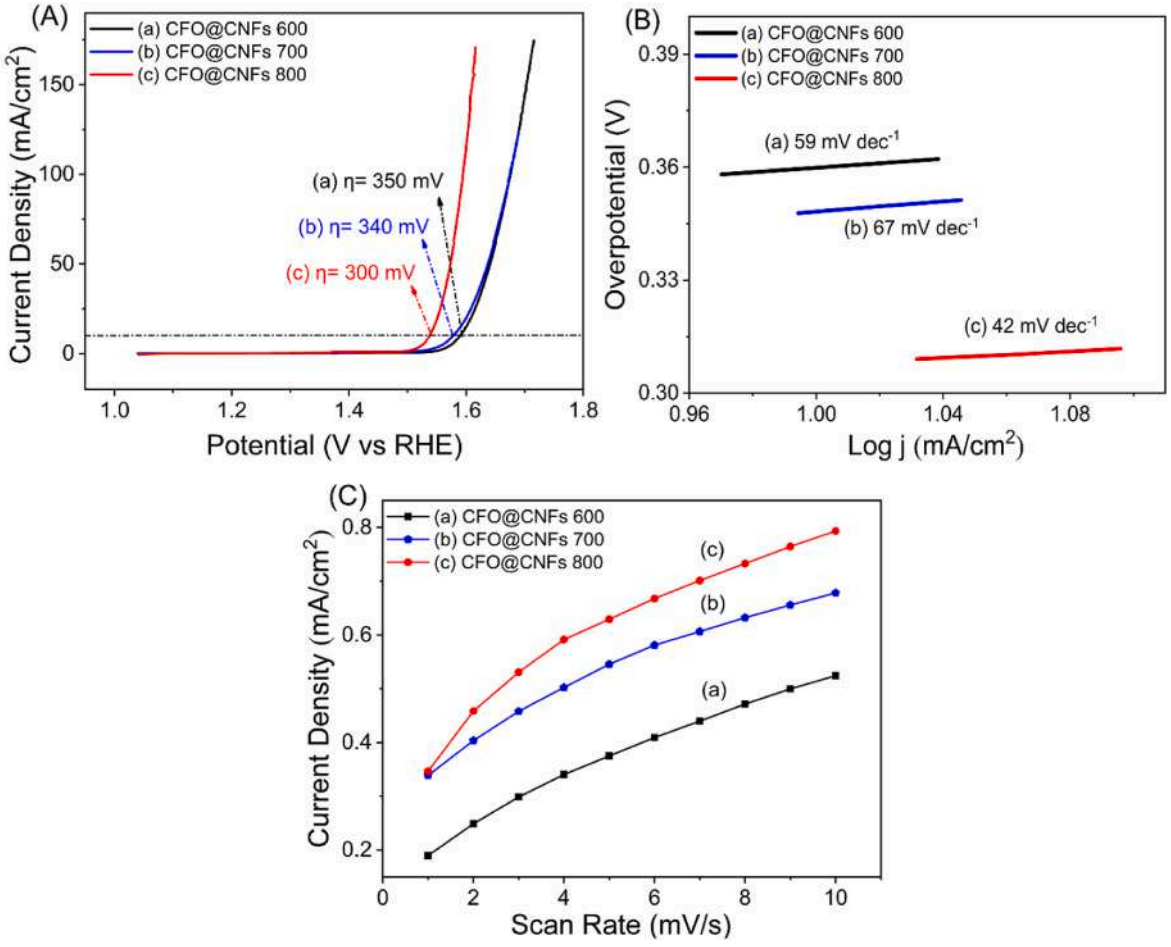

Fig. 6. iR-corrected LSV polarization curves at 1 mV/s scan rate (A), corresponding Tafel plots (B), and ECSA values (C) of CFO@CNFs 600, CFO@CNFs 700, and CFO@CNFs 800 for OER study.

consistent porosity, and the conductive properties of CNFs. The reduced overpotential observed for CFO@CNFs 800 is likely due to a combination of factors. The higher annealing temperature led to a decrease in fiber diameter as we can observed from SEM images, potentially resulting from the decomposition of the PAN polymer and the formation of a carbon matrix. The carbon matrix significantly enhances conductivity and reduces overpotential [26]. This carbon matrix may also have prevented nanoparticle aggregation, thereby increasing the number of exposed active sites. Additionally, the improved charge transfer within the carbon matrix could enhance the electrocatalytic performance, contributing to the lower overpotential [27]. Detailed overpotential and Tafel slope values of CFO@CNFs materials without iR correction are presented in Table S1 of SI. Notably, CFO@CNFs 800 demonstrated a significantly lower overpotential than CFO@CNFs 600 and CFO@CNFs 700, indicating superior electrocatalytic performance. This increased electrocatalytic performance is due to the increased crystallinity and high specific surface area [28]. Additionally, the carbon matrix that is preserved serves multiple purposes. This approach not only prevents the aggregation of active nanoparticles, maximizing their available reaction sites but also improves the transfer of electrical charge within the catalyst itself [29]. This augmentation is further supported by Tafel plots (Fig. 6B) explaining the nanomaterials' behaviour towards OER. The Tafel slopes for CFO@CNFs 600, CFO@CNFs 700, and CFO@CNFs 800 are found to be 56 mV dec^{-1}, 67 mV dec^{-1}, and 42 mV dec^{-1}, respectively. Notably, CFO@CNFs 800 exhibited a lower Tafel slope compared to CFO@CNFs 600 and CFO@CNFs 700, indicating faster reaction kinetics and higher OER activity. Typically, a lower Tafel slope recommends that the rate-determining step (RDS) is positioned closer to the conclusion of the multi-electron transfer reaction [30,31]. This suggests that CFO@CNFs 800 has a more efficient charge transfer process than the other catalysts investigated.

ECSA is an important parameter for assessing the active sites of electrocatalysts. ECSA was determined by measuring the C_{dl} through CV within a potential range usually between 0.1 and 0.3 V (Fig. S5). The C_{dl} is derived from the linear correlation between the anodic current (mA) and the scan rate (mV) as depicted in Fig. 6C. The C_{dl} values of CFO@CNFs 600, CFO@CNFs 700, and CFO@CNFs 800 were 0.03615 mF, 0.03659 mF, and 0.0457 mF. ECSA was determined using the equation [32],

$$ECSA = \frac{Cdl}{C_s} \quad [3]$$

The specific capacitance (C_S) employed is 0.040 mF/cm^2, which is typical of metal and ferrite-based electrodes in alkaline solutions. From the calculated C_{dl} values, the ECSA values are determined to be 0.90 cm^2, 0.91 cm^2, and 1.14 cm^2 for CFO@CNFs 600, CFO@CNFs 700, and CFO@CNFs 800, respectively. The higher ECSA of CFO@CNFs 800 indicates greater surface roughness and increased exposure of active sites, typically leading to enhanced electrocatalytic performance [33–35].

TOF stands as a key parameter in assessing the efficacy of electrocatalysts. It quantifies the rate at which species are generated and measured in moles per surface metal atom per second. TOF can be calculated using following equations [36],

$$TOF = \frac{j \times N_A}{n \times F \times \Gamma} \quad [4]$$

$$\Gamma = \frac{Peak\ area}{scan\ rate \times 1.69 \times 10^{-19}} \quad [5]$$

where j denotes the current density (in A/cm^2), N_A is Avogadro's number, n is the number of electrons involved in producing one molecule of the product (2 for H_2 and 4 for O_2), F represents Faraday constant (96 485 C/mol), and Γ symbolizes the surface concentration of active sites on the catalyst material, indicating the number of participating atoms involved in the reaction. The peak area required to calculate Γ was obtained from Fig. S6 of SI Fig. 7A shows a bar diagram illustrating TOF values with the inset showing a linear relationship between TOF and η during the OER regime. Increased catalytic activity is associated with a higher TOF. At a potential of 1.6 V, TOF values for CFO@CNFs 600, CFO@CNFs 700, and CFO@CNFs 800 are 0.92, 0.98, and 1.64 S^{-1}, respectively.

CFO@CNFs 800 sample demonstrates a favorable balance between low η and high TOF. The CFO@CNFs 800 catalyst also exhibits notable OER durability of 48 h at the current density of 10 mA/cm^2, as demonstrated in Fig. 8B. Moreover, the inset of Fig. 7B illustrates that the overpotential for CFO@CNFs 800 before and after stability changes only slightly, indicating minimal variation even after continuous catalysis for over 48 h. This consistency suggests the long-term stability of CFO@CNFs 800 towards the OER, likely due to the stable structure of the CFO@CNFs 800/Ni foam electrode. However, certain fluctuations observed during prolonged testing are attributable to the trapping and subsequent release of bubbles on the electrode surface [37].

To assess the charge transfer resistance of CFO@CNFs during OER, EIS measurements were conducted with a 10 mV applied amplitude over a frequency range of 10^5–0.01 Hz and corresponding Nyquist plots are depicted in Fig. 8A. The respective solution resistance (R_s) values for the CFO@CNFs 600, CFO@CNFs 700, and CFO@CNFs 800 electrocatalysts are found to be 1.9 Ω/cm^2, 1.8 Ω/cm^2, and 1.3 Ω/cm^2. Similarly, the charge transfer resistance (R_{ct}) values were measured as 10.3 Ω/cm^2, 5.2 Ω/cm^2, and 1.5 Ω/cm^2 for the CFO@CNFs 600, CFO@CNFs 700, and CFO@CNFs 800, respectively. These results suggest a considerably lower R_s and R_{ct} for CFO@CNFs 800, which correlates with improved OER performance [38]. This is due to favorable electrical conductivity and efficient channels of the CFO@CNFs 800. These characteristics accelerate electron transfer and hinder the aggregation of active components [39]. The impedance spectroscopy data were fitted using an equivalent circuit (Fig. S7) and it matches well with the experimental results. The experimental and circuit-fitted values of R_{ct} and R_s for CFO@CNFs are tabulated in Table S2. The Nyquist plots indicated that R_{ct} and R_s values for the CFO@CNFs 800 catalysts were notably smaller compared to that of other tested catalysts, indicating efficient OER kinetics at the interfaces between the electrode and electrolyte. The Bode plots shown in Fig. 8b reveal consistent patterns, with phase angles of 33.81°, 26.36°, and 16.49° observed for CFO@CNFs 600, CFO@CNFs 700, and CFO@CNFs 800, respectively. A lower phase angle typically signifies enhanced charge transfer across the interface and its superior performance in facilitating the OER [40]. The admittance values for

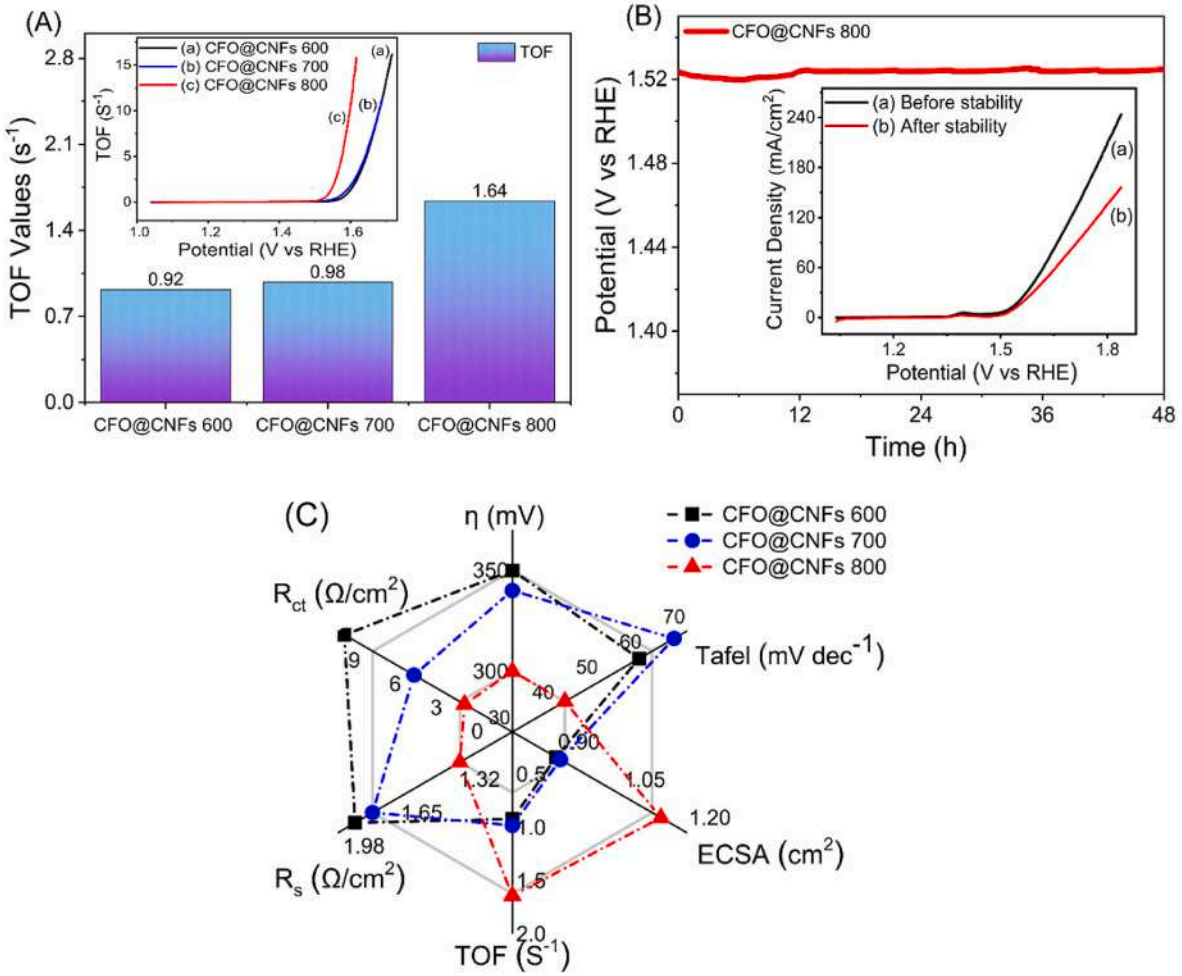

Fig. 7. (A) Bar diagram of TOF values for CFO@CNFs 600, CFO@CNFs 700, and CFO@CNFs 800 for electrocatalytic OER study. Inset shows TOF vs η plot during the OER regime for CFO@CNFs. (B) Chronopotentiometry curve of the CFO@CNFs 800 at the current density of 10 mA/cm^2 without iR correction. Inset shows LSV curves for CFO@CNFs 800 before and after 48 h stability. (C) Radar plot to compare overall OER performance of CFO@CNFs.

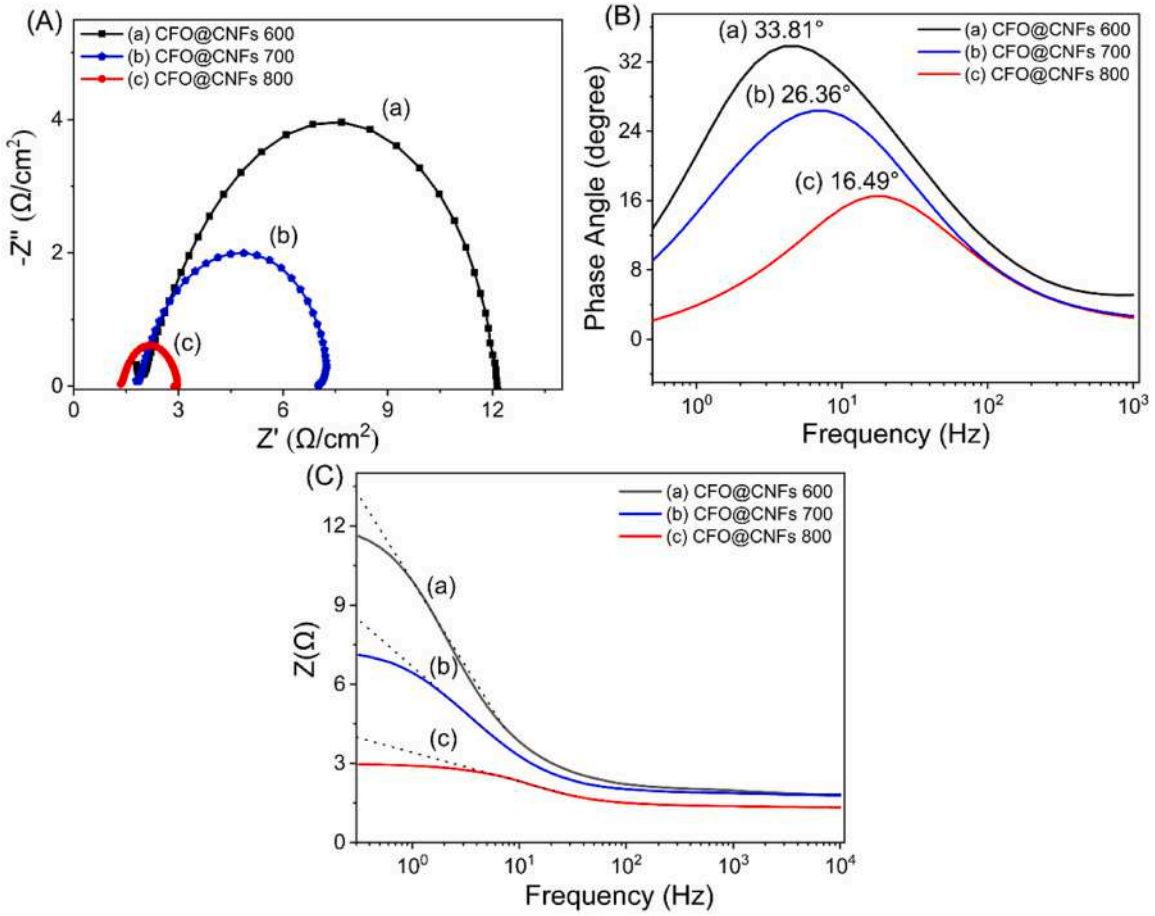

Fig. 8. (A) Nyquist plots, (B) Bode phase angle plots, and (C) bode absolute impedance plots of CFO@CNFs 600, CFO@CNFs 700, and CFO@CNFs 800.

CFO@CNFs 600, CFO@CNFs 700, and CFO@CNFs 800 were derived from their respective Bode absolute impedance plots (Fig. 8c). Admittance, being the reciprocal of impedance modulus, primarily reflects the ease with which electrons can traverse an interface, particularly at lower frequencies. Therefore, higher admittance values indicate superior activity. As expected, CFO@CNFs 800 demonstrated a higher admittance (0.25 S) compared to CFO@CNFs 700 (0.11 S) and CFO@CNFs 600 (0.07 S) underscoring its enhanced performance. The enhanced electrocatalytic performance of CFO@CNFs 800 results from the synergistic electronic interactions between metal oxide ions and the fibrous structure. The carbon matrix improves electrical conductivity and prevents nanoparticle aggregation. The OER performance of the CFO@CNFs 800 catalyst is compared against other similar catalysts previously reported (Table S3). The results demonstrate that the CFO@CNFs 800 catalyst exhibits superior or comparable electrocatalytic performance compared to many of these reported catalysts.

4. Conclusions

Metal-organic framework derived CFO NPs embedded carbon nanofibers (CFO@CNFs) were successfully synthesized in a two-step process which includes hydrothermal and electrospinning methods. The synthesized NFs were calcined at 600 °C, 700 °C, and 800 °C temperatures in the N_2 atmosphere and applied as an OER electrocatalyst. The XRD results show that the crystallinity of the CFO@CNFs increases with increasing calcination temperature. The FESEM and TEM results show the fibrous morphology of CNFs along with the decorated MOF-derived CFO NPs. Varying the calcination temperature led to changes in the morphology of the CFO@CNFs. CFO@CNFs 800 exhibited enhanced OER catalytic activity with lower overpotential compared to CFO@CNFs 600 and CFO@CNFs 700. Also, CFO@CNFs 800 shows a low tafel slope of 42 mV dec^{-1} and a high ECSA of 1.14 cm^2. Such enhanced electrocatalytic performance of CFO@CNFs 800 was due to the synergistic electronic interactions between the metal oxide ions along with the fibrous structure. Moreover, the preserved carbon matrix within the CFO@CNFs 800 catalyst not only enhances electrical conductivity but also prevents nanoparticle aggregation. This characteristic gives the catalyst exceptional durability of over 48 h in OER. These findings give more insights for a rational design to make efficient catalysts based on MOF-derived NPs decorated on conductive nanofibers for water-splitting reactions as well as other energy-related applications.

CRediT authorship contribution statement

T.P. Kamble: Writing – original draft. **S.R. Shingte:** Writing – original draft, Formal analysis. **V.D. Chavan:** Formal analysis. **Deok-Kee Kim:** Visualization. **S.H. Mujawar:** Formal analysis. **T.D. Dongale:** Visualization, Supervision, Data curation. **P.B. Patil:** Writing – review & editing, Supervision, Project administration, Investigation, Conceptualization.

Declaration of competing interest

The authors declare that they have no known competing financial interests or personal relationships that could have appeared to influence the work reported in this paper.

Acknowledgments

This work is supported by the Diamond Jubilee Research Initiation

Scheme 2022–2023 (no. SU/C&U.D.S./2022–2023/25/412). V.D. Chavan and Deok-Kee Kim acknowledge the financial support provided by the National Research Foundation of Korea (NRF), funded by the Ministry of Science and ICT (2016R1D1A1B01009537).

Appendix A. Supplementary data

Supplementary data to this article can be found online at https://doi.org/10.1016/j.ijhydene.2024.10.353.

References

[1] Bu Y, et al. A highly efficient composite cathode for proton-conducting solid oxide fuel cells. J Power Sources October 2019;451:227812. https://doi.org/10.1016/j.jpowsour.2020.227812. 2020.
[2] Yuan CZ, et al. One-step in situ growth of iron–nickel sulfide nanosheets on FeNi alloy foils: high-performance and self-supported electrodes for water oxidation. Small 2017;13(18):1–8. https://doi.org/10.1002/smll.201604161.
[3] Zhou Y, Fan HJ. Progress and challenge of amorphous catalysts for electrochemical water splitting. Am Chem Soc Jan. 04, 2021. https://doi.org/10.1021/acsmaterialslett.0c00502.
[4] Anantharaj S, Noda S. Amorphous catalysts and electrochemical water splitting: an untold story of harmony. Wiley-VCH Verlag; Jan. 01, 2020. https://doi.org/10.1002/smll.201905779.
[5] Hu C, Zhang L, Gong J. Recent progress made in the mechanism comprehension and design of electrocatalysts for alkaline water splitting. Energy Environ Sci Sep. 2019;12(9):2620–45. https://doi.org/10.1039/c9ee01202h.
[6] Anantharaj S, Kundu S. Do the evaluation parameters reflect intrinsic activity of electrocatalysts in electrochemical water splitting? Am Chem Soc 2019;Jun. 14. https://doi.org/10.1021/acsenergylett.9b00686.
[7] Kim BK, Kim MJ, Kim JJ. Impact of surface hydrophilicity on electrochemical water splitting. ACS Appl Mater Interfaces Mar. 2021;13(10):11940–7. https://doi.org/10.1021/acsami.0c22409.
[8] Ayyappan S, Mahadevan S, Chandramohan P, Srinivasan MP, Philip J, Raj B. Influence of Co^{2+} Ion concentration on the size, magnetic properties, and purity of $CoFe_2O_4$ Spinel ferrite nanoparticles. J Phys Chem C Apr. 2010;114(14):6334–41. https://doi.org/10.1021/jp911966p.
[9] Rana S, Yadav KK, Guchhait SK, Nishanthi ST, Mehta SK, Jha M. Insights of enhanced oxygen evolution reaction of nanostructured cobalt ferrite surface. J Mater Sci May 2021;56(14):8383–95. https://doi.org/10.1007/s10853-020-05629-9.
[10] Li M, et al. Facile synthesis of electrospun MFe_2O_4 (M = Co, Ni, Cu, Mn) spinel nanofibers with excellent electrocatalytic properties for oxygen evolution and hydrogen peroxide reduction. Nanoscale May 2015;7(19):8920–30. https://doi.org/10.1039/c4nr07243j.
[11] Ma TY, Dai S, Jaroniec M, Qiao SZ. Metal-organic framework derived hybrid Co_3O_4-carbon porous nanowire arrays as reversible oxygen evolution electrodes. J Am Chem Soc Sep. 2014;136(39):13925–31. https://doi.org/10.1021/ja5082553.
[12] Shen K, Chen X, Chen J, Li Y. Development of MOF-derived carbon-based nanomaterials for efficient catalysis. Am Chem Soc Sep. 02, 2016. https://doi.org/10.1021/acscatal.6b01222.
[13] Ye L, et al. Highly efficient porous carbon electrocatalyst with controllable N-species content for selective CO_2 reduction. Angew Chem Int Ed Feb. 2020;59(8):3244–51. https://doi.org/10.1002/anie.201912751.
[14] Qin L, Xu Z, Zheng Y, Li C, Mao J, Zhang G. Confined transformation of organometal-encapsulated MOFs into spinel $CoFe_2O_4$/C nanocubes for low-temperature catalytic oxidation. Adv Funct Mater Apr. 2020;30(14). https://doi.org/10.1002/adfm.201910257.
[15] Xue F, et al. Engineering flexible carbon nanofiber concatenated MOF-derived hollow octahedral $CoFe_2O_4$ as an anode material for enhanced lithium storage. Inorg Chem Front Jul. 2021;8(13):3363–70. https://doi.org/10.1039/d1qi00414j.
[16] Xue F, et al. Engineering flexible carbon nanofiber concatenated MOF-derived hollow octahedral $CoFe_2O_4$ as an anode material for enhanced lithium storage. Inorg Chem Front Jul. 2021;8(13):3363–70. https://doi.org/10.1039/d1qi00414j.
[17] Londoño-Restrepo SM, Millán-Malo BM, del Real-López A, Rodriguez-García ME. In situ study of hydroxyapatite from cattle during a controlled calcination process using HT-XRD. Mater Sci Eng C 2019;105(Dec). https://doi.org/10.1016/j.msec.2019.110020.
[18] Patil PD, et al. Effect of annealing temperature on morphologies of metal organic framework derived $NiFe_2O_4$ for supercapacitor application. J Energy Storage 2021;40(Aug). https://doi.org/10.1016/j.est.2021.102821.
[19] Hou C, Chen W, Fu L, Zhang S, Liang C, Wang Y. Efficient degradation of perfluorooctanoic acid by electrospun lignin-based bimetallic MOFs nanofibers composite membranes with peroxymonosulfate under solar light irradiation. Int J Biol Macromol Mar. 2021;174:319–29. https://doi.org/10.1016/j.ijbiomac.2021.01.184.
[20] Chen IH, Wang CC, Chen CY. Fabrication and characterization of magnetic cobalt ferrite/polyacrylonitrile and cobalt ferrite/carbon nanofibers by electrospinning. Carbon N Y Mar. 2010;48(3):604–11. https://doi.org/10.1016/j.carbon.2009.09.062.
[21] Sun B, et al. Pseudocapacitive Li^+ storage boosts ultrahigh rate performance of structure-tailored $CoFe_2O_4$@Fe_2O_3 hollow spheres triggered by engineered surface and near-surface reactions. Nano Energy 2019;66(Dec). https://doi.org/10.1016/j.nanoen.2019.104179.
[22] Wang C, et al. Coordination polymers-derived three-dimensional hierarchical $CoFe_2O_4$ hollow spheres as high-performance lithium ion storage. ACS Appl Mater Interfaces Aug. 2018;10(34):28679–85. https://doi.org/10.1021/acsami.8b09459.
[23] Li D, Li G, Ge H, Zhang J, Meng X. Fabrication of $CoFe_2O_4$ and $NiFe_2O_4$ nanoporous spheres as promising anodes for high performance lithium-ion batteries. New J Chem 2017;41(24):15501–7. https://doi.org/10.1039/c7nj03324a.
[24] Chakrapani K, et al. Role of composition and size of cobalt ferrite nanocrystals in the oxygen evolution reaction. ChemCatChem Aug. 2017;9(15):2988–95. https://doi.org/10.1002/cctc.201700376.
[25] Silva VD, Ferreira LS, Simões TA, Medeiros ES, Macedo DA. 1D hollow MFe_2O_4 (M = Cu, Co, Ni) fibers by Solution Blow Spinning for oxygen evolution reaction. J Colloid Interface Sci Mar. 2019;540:59–65. https://doi.org/10.1016/j.jcis.2019.01.003.
[26] A study on electrical resistivity behaviors of PAN-based carbon nanofiber webs".
[27] Zhong M, Yan S, Xu J, Wang C, Lu X. Manipulating Ru oxidation within electrospun carbon nanofibers to boost hydrogen and oxygen evolution for electrochemical overall water splitting. Inorg Chem Front Aug. 2022;9(19):4881–91. https://doi.org/10.1039/d2qi01168a.
[28] Fang W, et al. Metal-organic framework derived Fe-Co-CN/reduced graphene oxide for efficient HER and OER. Electrochim Acta 2021;365(Jan). https://doi.org/10.1016/j.electacta.2020.137384.
[29] Zhong M, Song N, Li C, Wang C, Chen W, Lu X. Controllable growth of Fe-doped NiS_2 on NiFe-carbon nanofibers for boosting oxygen evolution reaction. J Colloid Interface Sci May 2022;614:556–65. https://doi.org/10.1016/j.jcis.2022.01.134.
[30] Zhong M, Yan S, Xu J, Wang C, Lu X. Manipulating Ru oxidation within electrospun carbon nanofibers to boost hydrogen and oxygen evolution for electrochemical overall water splitting. Inorg Chem Front Aug. 2022;9(19):4881–91. https://doi.org/10.1039/d2qi01168a.
[31] Shinagawa T, Garcia-Esparza AT, Takanabe K. Insight on Tafel slopes from a microkinetic analysis of aqueous electrocatalysis for energy conversion. Sci Rep 2015;5(May):1–21. https://doi.org/10.1038/srep13801.
[32] Dalai N, Mohanty B, Mitra A, Jena B. Highly active ternary nickel–iron oxide as bifunctional catalyst for electrochemical water splitting. ChemistrySelect Jul. 2019;4(27):7791–6. https://doi.org/10.1002/slct.201901465.
[33] Voiry D, et al. Best practices for reporting electrocatalytic performance of nanomaterials. ACS Nano 2018;12(10):9635–8. https://doi.org/10.1021/acsnano.8b07700.
[34] Dinh KN, et al. Electronic modulation of nickel disulfide toward efficient water electrolysis. Small 2020;16(17):1–9. https://doi.org/10.1002/smll.201905885.
[35] Liu C, et al. (NiFe)S_2 nanoparticles grown on graphene as an efficient electrocatalyst for oxygen evolution reaction. Electrochim Acta 2018;286:195–204. https://doi.org/10.1016/j.electacta.2018.08.015.
[36] Karthick K, Anantharaj S, Karthik PE, Subramanian B, Kundu S. Self-assembled molecular hybrids of CoS-DNA for enhanced water oxidation with low cobalt content. Inorg Chem Jun. 2017;56(11):6734–45. https://doi.org/10.1021/acs.inorgchem.7b00855.
[37] Rebekah A, Anantharaj S, Viswanthan C, Ponpandian N. Zn-substituted $MnCo_2O_4$ nanostructure anchored over rGO for boosting the electrocatalytic performance towards methanol oxidation and oxygen evolution reaction (OER). Int J Hydrogen Energy May 2020;45(29):14713–27. https://doi.org/10.1016/j.ijhydene.2020.03.231.
[38] Gao X, et al. Ru/RuO_2Nanoparticle composites with N-doped reduced graphene oxide as electrocatalysts for hydrogen and oxygen evolution. ACS Appl Nano Mater Dec. 2020;3(12):12269–77. https://doi.org/10.1021/acsanm.0c02739.
[39] Zhang L, et al. Recent advances in 1D electrospun nanocatalysts for electrochemical water splitting. John Wiley and Sons Inc; Feb. 01, 2021. https://doi.org/10.1002/sstr.202000048.
[40] Anantharaj S, Sugime H, Noda S. Why shouldn't double-layer capacitance (C_{dl}) Be always trusted to justify faradaic electrocatalytic activity differences?. 2021.